Optical spin-to-orbital angular momentum conversion in the near field of a highly nonparaxial optical field with hybrid states of polarization

Rui-Pin Chen,[1,*] Khian-Hooi Chew,[2] Chao-Qing Dai,[3] and Guoquan Zhou[3]
[1]*Department of Physics, Zhejiang Sci-Tech University, Hangzhou 310018, China*
[2]*Center for Theoretical Physics, Department of Physics, Faculty of Science, University of Malaya, Kuala Lumpur 50603, Malaysia*
[3]*School of Sciences, Zhejiang A & F University, Linan 311300, China*
(Received 13 July 2017; published 29 November 2017)

The conversion of the spin-to-orbital optical angular momentum (AM) of an optical field with hybrid states of polarization (SOP) in the near-field region is studied based on the angular spectrum method. The spin-to-orbital optical AM conversion occurs in the longitudinal component of an optical field with hybrid SOP under a highly nonparaxial circumstance. The longitudinal component exhibits different phases and intensity distributions compared to that of the transverse component and it depends sensitively on the initial SOP. Our study reveals that the density distribution of the converted orbital AM can be spatially manipulated by controlling the initial state of polarization.

DOI: 10.1103/PhysRevA.96.053862

I. INTRODUCTION

Light carries angular momentum (AM) that comprises of both a spin component associated with the circular polarization and an orbital component arising from the spatially spiral profile of the phase in the field cross section [1,2] has attracted immense attention due to their fundamental interest and potential applications [3–6]. The interplay between the spin AM and the orbital AM, especially the conversion and interaction of spin and orbital AMs in different materials [7–18], remains a challenging topic in the corresponding fields with many applications such as the surface plasmon optical tweezers [13] and the light-driven plasmonic motors [14]. The conversion of the spin-to-orbital AM has been extensively studied using the especially designed optical devices such as the q-plate devices [15], nanostructure materials [16], the interferometric schemes [17], and nonlinear optic techniques [18]. The spin-to-orbital AM conversion in a strongly focusing circularly polarized beam has been reported [19]. As a special case of a highly nonparaxial beam, a strongly focusing beam can redirect the circular polarization and generate the longitudinal component. Furthermore, the spiral phase created in the longitudinal component leads to the formation of orbital AM since there is a phase difference of $\pi/2$ between the x and y components in the circular polarization. In the near field, however, the evanescent wave [20–22] component cannot be neglected; it even dominates the field under a highly nonparaxial circumstance, and it attenuates exponentially with increasing distance. The nonparaxial property of the evanescent wave can redirect the polarizations and generate the longitudinal component. Compared to a scalar beam with uniform polarization distribution in the field cross section, the vector optical field with hybrid stats of polarization (SOP) exhibits various polarizations such as linear, circular, and elliptical polarization that are located at different positions of the field cross section [23–28]. Since the spin-to-orbital AM conversion can occur in a nonparaxial beam with a circular polarization [19], the spin-to-orbital AM conversion is expected to occur in the longitudinal component in the near field of a nonparaxial light field with hybrid SOP. A three-dimensional (3D) polarization structure or a 3D intensity structure may also appear in the near field of a highly nonparaxial beam with hybrid SOP. Although the manipulation and application of the evanescent wave have been reported in many works [29–33], the studies pertaining to the variety of the longitudinal component profile distribution in the near field resulting from the hybrid SOP is still scarce. Nonetheless, the spin-to-orbital optical AM conversion and its manipulation in the near field of a highly nonparaxial beam with hybrid SOP are scarcely known and its exploration is still in its infancy.

In this work, the spin-to-orbital AM conversion in the near field of a highly nonparaxial beam with hybrid SOP is studied within the framework of the angular spectrum method [32–34]. In particular, the longitudinal component of an evanescent wave plays an important role in the spin-to-orbital AM conversion in near field. The propagation dynamics of a highly nonparaxial beam with hybrid SOP in the near field are studied analytically by including the propagating and the evanescent waves. The propagating and evanescent waves are decomposed into transverse and longitudinal components. The spatial shape of these components and the ratios between their respective contributions are numerically obtained. The intensity distributions of the vector optical field in the near-field region are found to be strongly dependent on the spatial distribution of SOP in the cross section of the field. In particular, the shapes of the intensity distribution of the longitudinal components are different from that of the transverse components, and they depend sensitively on the spatial distribution of SOP in the field cross section. The evanescent wave dominates the field in the near field, giving rise to a variety of shapes in the field distribution. It is found that the spin-to-orbital AM conversion always occurs in the longitudinal component of both the evanescent and propagating waves. This work may provide useful information on how to spatially manipulate the spin-to-orbital AM conversion in the near field of a highly nonparaxial beam by choosing the initial SOPs in the field's cross section.

II. THEORY

We consider the propagation dynamics of a Gaussian beam with a hybrid SOP in the field cross section in the Cartesian

*Corresponding author: chenrp@zstu.edu.cn

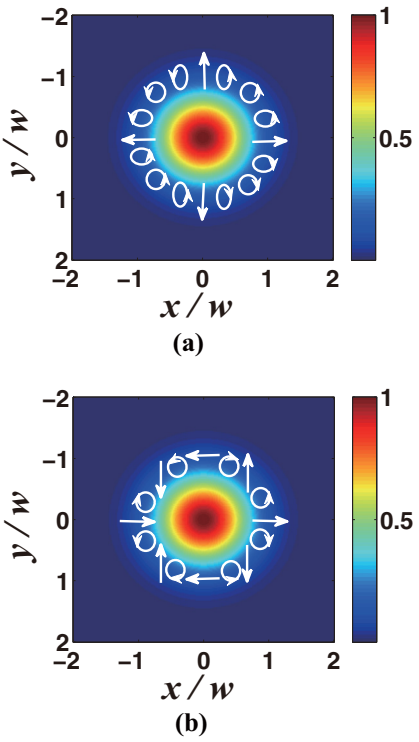

FIG. 1. Hybrid SOP distributions in the cross sections of an optical field for different numbers of polarization topological charge: (a) $m = 1$; (b) $m = 2$. The initial phase $\theta_0 = 0$ and the intensity distributions have been normalized to the peak intensity.

coordinate system. The z axis is taken to be the propagation axis [23–25]

$$E(r,\theta) = \exp(-r^2/w^2)[\cos(m\theta+\theta_0)e_x + \exp(i\,\Delta\theta)\sin(m\theta+\theta_0)e_y], \quad (1)$$

where $r = \sqrt{x^2+y^2}$ and $\theta = \arctan(y/x)$ represent the polar radius and azimuthal angle in the polar coordinate system, respectively. w is the beamwidth. e_x and e_y are the unit vectors in the x and y direction, respectively. If $\Delta\theta = 0$, the x and y components have the same phase. In this case, the SOP depends only on the azimuthal angle θ and the vector optical field which is linearly polarized in different directions in the field cross section. For the case of $m = 1$ with $\theta_0 = 0$ and $\pi/2$, the vector fields describe the radially and azimuthally polarized fields, respectively. Equation (1) degenerates to the linearly polarized fields, if $m = 0$. However, for the case with $\Delta\theta \neq 0$ [Eq. (1)], the x and y components possess different phases, implying a hybrid-polarized vector field with the linear, circular, and elliptical polarization states located at different positions in the field's cross section. In Fig. 1, we show the hybrid SOP distributions in the cross sections of an optical field for different numbers of polarization topological charge with $\Delta\theta = \pi/2$. The structured hybrid SOP has been experimentally generated [23–26]. It should be noted that the hybrid SOP distributions are generated in the cross section of an expanding incident beam (i.e., with uniform amplitude) [23–26]. If the incident beam is replaced by a Gaussian beam, the vector optical field described by Eq. (1) will be generated. By using the Fourier transform, the transverse components of the vector angular spectrum $\tilde{E}_x(\rho\cos\varphi,\rho\sin\varphi)$ and $\tilde{E}_y(\rho\cos\varphi,\rho\sin\varphi)$ of the initial field are given by [32,33]

$$\begin{pmatrix}\tilde{E}_x(\rho\cos\varphi,\rho\sin\varphi)\\ \tilde{E}_y(\rho\cos\varphi,\rho\sin\varphi)\end{pmatrix} = \left(\frac{k}{2\pi}\right)^2 \begin{pmatrix}\int_0^\infty\int_0^{2\pi}\exp(-r^2/w^2)\cos(m\theta+\theta_0)\exp[-ikr\rho\cos(\theta-\varphi)]r\,d\theta\,dr\\ \int_0^\infty\int_0^{2\pi} i\,\exp(-r^2/w^2)\sin(m\theta+\theta_0)\exp[-ikr\rho\cos(\theta-\varphi)]r\,d\theta\,dr\end{pmatrix}, \quad (2)$$

where k is the wave number. ρ and φ are the Fourier plane coordinates in the polar coordinate representation. The relationship of ρ and φ to the transverse Cartesian Fourier-transform variables μ and ν are $\mu = \rho\cos\varphi$, $\nu = \rho\sin\varphi$, and $\gamma = \sqrt{1-\rho^2}$, where μ, ν, and γ denote the direction cosines. If $\rho < 1$, $\gamma = \sqrt{1-\rho^2}$ corresponds to propagating (homogeneous) plane waves at angles $\cos^{-1}\gamma$ (or $\sin^{-1}\rho$) with respect to the z axis, whereas $\gamma = i\sqrt{\rho^2-1}$ gives evanescent plane waves, if $\rho \geqslant 1$. Thus the angular spectrum is described by

$$A(\rho\cos\phi,\rho\sin\phi) = \left(\frac{k}{2\pi}\right)^2 \frac{\sqrt{\pi}kw^3\rho\pi i^m}{4}\exp(-k^2w^2\rho^2/8)[I_{(m-1)/2}(k^2w^2\rho^2/8) - I_{(m+1)/2}(k^2w^2\rho^2/8)][\cos(m\phi+\theta_0)e_x + i\,\sin(m\phi+\theta_0)e_y - [\cos(m\phi+\theta_0)\cos\phi + i\,\sin(m\phi+\theta_0)\sin\phi]\rho/\gamma e_z], \quad (3)$$

where $I_\alpha(.)$ is the Bessel function of the second kind of order α; e_z is the unit vector in z direction. The electric-field component of the cylindrical vector optical field in z plane can be represented as

$$E(r) = (-1)^m\frac{k^3w^3\sqrt{\pi}}{8}\int_0^\infty e^{-k^2w^2\rho^2/8}P\{J_m(-kr\rho)[\cos(m\theta+\theta_0)e_x + i\,\sin(m\theta+\theta_0)e_y] - [J_{m+1}(-kr\rho)\cos(m\theta+\theta+\theta_0)(i-1) + J_{m-1}(-kr\rho)\cos(m\theta-\theta+\theta_0)(1+i)]\rho/(2\gamma)e_z\}\exp(ik\gamma z)\rho^2 d\rho, \quad (4)$$

where $J_\beta(.)$ denotes the Bessel function of the first kind of order β; $P = I_{(m-1)/2}(k^2w^2\rho^2/8) - I_{(m+1)/2}(k^2w^2\rho^2/8)$. When $m = 0$, $\theta_0 = \pi/4$, thus $P = 4\exp(-k^2w^2\rho^2/8)/(\pi^{1/2}kw\rho)$; Eq. (2) is degenerated for a scalar optical field with the uniform circular polarization in the field cross section:

$$E(r) = \frac{k^2w^2}{2}\int_0^\infty e^{-k^2w^2\rho^2/4}[J_0(-kr\rho)(e_x+ie_y) - iJ_1(-kr\rho)\exp(i\theta)\rho/\gamma e_z]\exp(ik\gamma z)\rho\,d\rho. \quad (5)$$

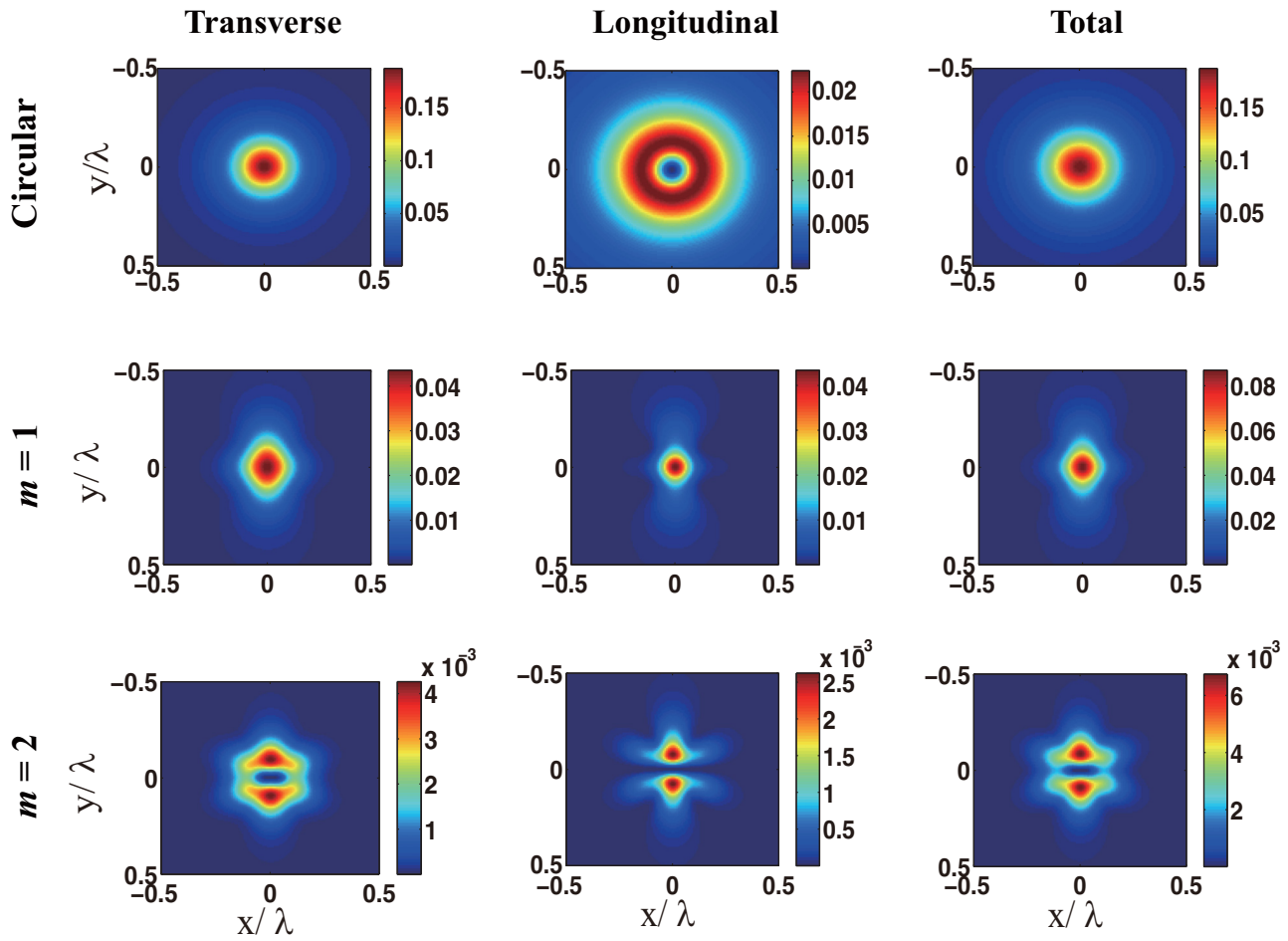

FIG. 2. Transverse, longitudinal, and total intensity distributions with different topological charge number of polarization. The waist size $w = 0.1\lambda$ and propagation distance $z = 0.1\lambda$. Here $\theta_0 = 0$ and $\Delta\theta = \pi/2$ for $m = 1$ and 2 for the hybrid SOP. Here the coordinate unit is wavelength λ. The intensity distributions have been normalized to the initial peak intensity.

For the case of $\rho < 1$, Eq. (4) describes the propagating waves $E_{\rm pr}$, whereas the equation gives the evanescent waves $E_{\rm ev}$, if $\rho \geqslant 1$.

The numerical integration is taken for the distributions of the intensity in Eq. (4). The results for the vector optical field with a waist size of $w = 0.1\lambda$ for a different topological number of polarization m at the propagation distance $z = 0.1\lambda$ are depicted in Fig. 2. In the figure, $\theta_0 = 0$ and $\Delta\theta = \pi/2$ for $m = 1$ and 2 for the hybrid SOP are as shown in the second and third rows in Fig. 2. It should be noted that the distributions of the longitudinal components are different from their transverse components.

The transverse energy (TE) flow of the vector cylindrical optical field in the xy plane where $z = \text{const}$ can be written in the following form:

$$S = \frac{1}{2}\mathrm{Re}[E(r)\times H^*(r)] = \frac{1}{2\mu_0\omega}\mathrm{Im}[E(r)\times(\nabla \times E(r)^*)], \tag{6}$$

where Re[.] and Im[.] represent the real and imaginary parts, respectively, and the asterisk corresponds to its complex conjugation. μ_0 and ω are the vacuum permeability and angular frequency, respectively. The separation of the orbital and spin AM from the total optical AM has been intensively demonstrated in the context of both paraxial and nonparaxial beams [35–41]. Recently, it has been pointed out by Bialynicki-Birula [39,40] that the orbital and the spin AM cannot be expressed as integrals of local densities. Their study reveals that the orbital AM and the spin are intrinsically macroscopic nonlocal objects. Here we separate the orbital and spin angular momentum densities of the optical field as [38–41]

$$J_z \propto \mathrm{Im}[r \times (E^* \cdot (\nabla)E)] \cdot e_z, \tag{7}$$

$$S_z \propto \mathrm{Im}[E^* \times E] \cdot e_z, \tag{8}$$

where J_z and S_z describe the z components of the orbital and spin AM density, respectively.

The numerical results for the distributions of the TE flux density, spin, and orbital AMs calculated by Eqs. (6) and (7) with the waist size $w = 0.1\lambda$ at a propagation distance of $z = 0.1\lambda$ for different topological number of polarizations m are depicted in Fig. 3. The second and third rows in Fig. 3 are respectively responsible for the hybrid SOP with $m = 1$ and 2 by setting $\theta_0 = 0$, $\Delta\theta = \pi/2$. It should be noted that the energy flux density and orbital AM are induced by the longitudinal components, as recognized from Eqs. (4) and (5). The results

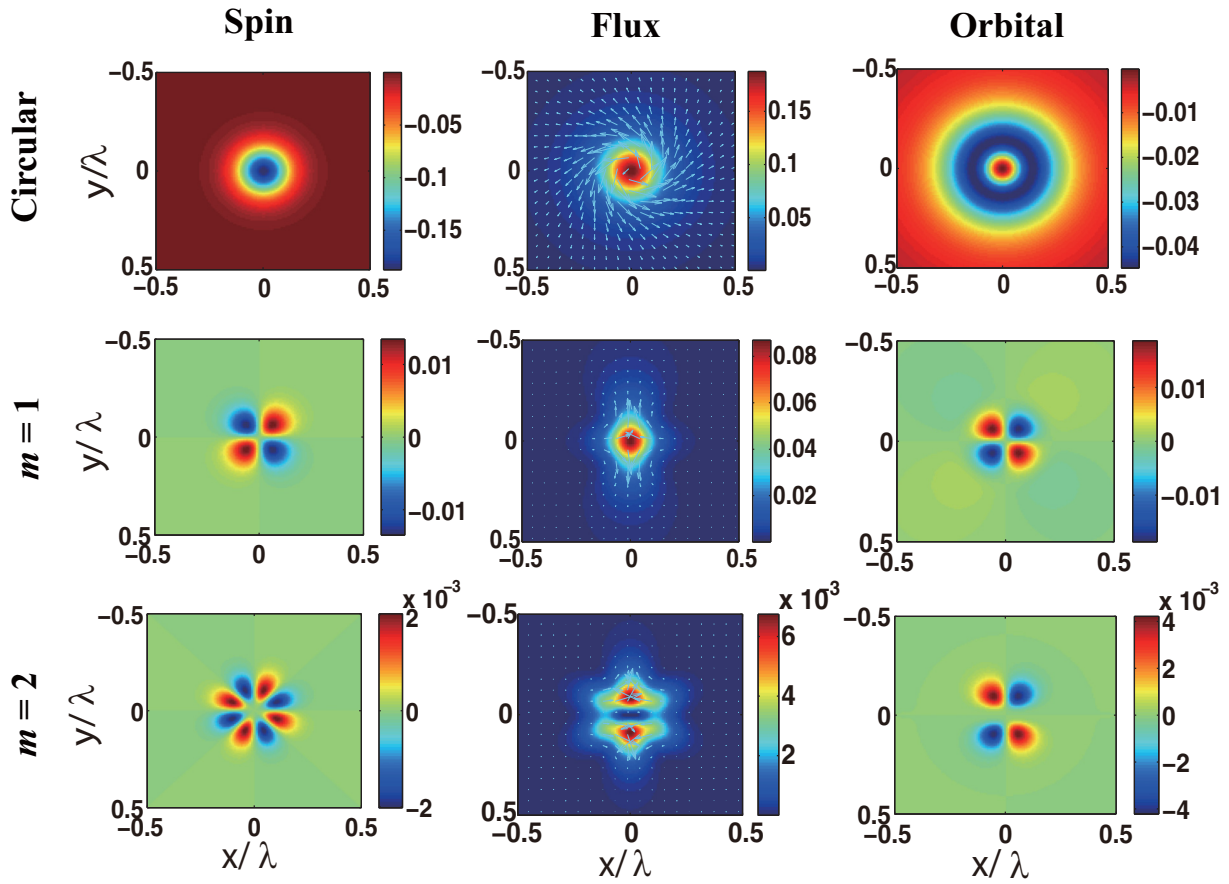

FIG. 3. Distributions of the spin momentum, energy flux density, and orbital momentum with different topological charge number of polarization. In the calculation, the parameters adopted are similar to that in Fig. 2.

indicate that the spin-orbital AM conversion occurs in the longitudinal components when the initial field is circularly polarized, as shown in Fig. 3 (first row). If $m = 1$, it is seen that there are four circular polarization components located at four different azimuthal positions and the spin-to-orbital AM conversions take place at the corresponding positions of the longitudinal component, as shown in Fig. 3. On the other hand, there are eight different azimuthal positions with the circular polarization if $m = 2$. The superpositions of the orbital AM converted from the spin AM in the longitudinal direction lead to an irregular distribution of orbital AM. This can be confirmed from the transverse energy flux density distribution, as depicted in Fig. 3.

III. CONTRIBUTIONS OF THE LONGITUDINAL COMPONENT OF EVANESCENT WAVES IN THE NEAR FIELD

At a highly nonparaxial circumstance, the contribution of the propagating and evanescent wave components can be compared in terms to the plane-integrated intensity (squared modulus) of the propagating $I_{\rm pr}$ and evanescent fields $I_{\rm ev}$ [32,33,42–44] as $I_{\rm pr} = \iint |E_{\rm pr}|^2 dx\, dy = \int_0^1 \int_0^{2\pi} [|a|^2 + |b|^2]\rho\, d\rho\, d\varphi$, $I_{\rm ev} = \iint |E_{\rm ev}|^2 dx\, dy = \int_1^\infty \int_0^{2\pi} [|a|^2 + |b_{\rm ev}|^2] \exp(-2kz\sqrt{\rho^2-1})\rho\, d\rho\, d\varphi$, where $a = \tilde{E}(\rho,\varphi)\cdot e_1$, $b = \tilde{E}(\rho,\varphi)\cdot e_2$, $b_{\rm ev} = \tilde{E}(\rho,\varphi)\cdot e_{\rm ev}$ and $e_1 = (\sin\varphi, \cos\varphi, 0)$, $e_2 = [(1-\rho^2)^{1/2}\cos\varphi, (1-\rho^2)^{1/2}\sin\varphi, -\rho]$, $e_{\rm ev} = [i(\rho^2-1)^{1/2}\cos\varphi, i(\rho^2-1)^{1/2}\sin\varphi, -\rho]/(2\rho^2-1)^{1/2}$.

Integrations of $I_{\rm pr}$ and $I_{\rm ev}$ over φ lead to a single variable ρ integral as follows:

$$I_{\rm pr} = 2\pi \int_0^1 |T|^2 |P|^2 (2-\rho^2)\rho/(1-\rho^2) d\rho, \tag{9}$$

$$I_{\rm ev} = 2\pi \int_1^\infty \frac{|T|^2 |P|^2 \rho (2\rho^4 - 3\rho^2 + 2)\exp(-2kz\sqrt{\rho^2-1})}{2\rho^4 - 3\rho^2 + 1} d\rho, \tag{10}$$

where $T = i^m (2\pi^{5/2}\rho w^3/8\lambda^3)\exp(-k^2\rho^2 w^2/8)$. The ratio $I_{\rm ev}/(I_{\rm pr} + I_{\rm ev})$ for a highly nonparaxial case of $w = 0.1\lambda$ with a different number of topological charges m as a function of the propagation distance z are illustrated in Fig. 4(a). It is clearly seen that the evanescent wave component $I_{\rm ev}$ dominates the near field and it drastically decreases with an increasing propagation distance. Upon further increase in the propagation distance above $z = 0.5\lambda$, $I_{\rm ev}$ continues to decay and approaches zero. Thus the contribution of the evanescent waves can be neglected for $z > 0.5\lambda$. As the number of topological charge m increases, it is found that $I_{\rm ev}$ increases. This is because the inhomogeneous distributions of x and y components [i.e., $\cos(m\theta)$ and $\sin(m\theta)$] lead to the

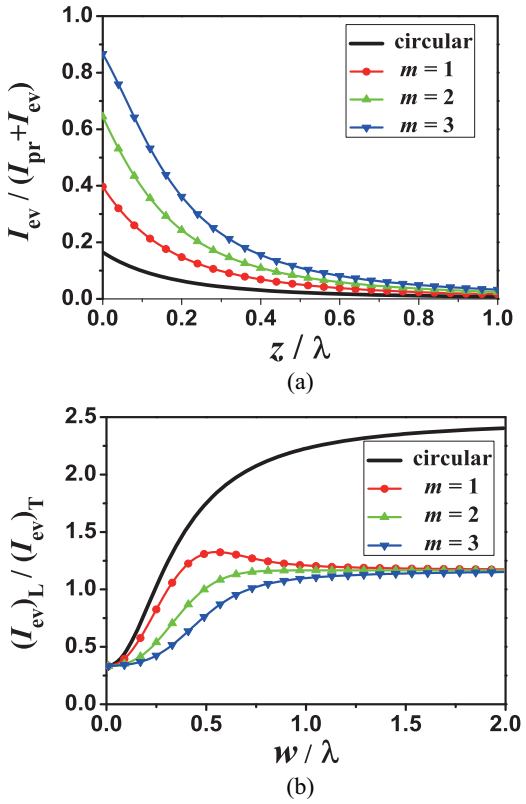

FIG. 4. Ratio of the plane-integrated intensity of different components for different number of polarization topological charges m: (a) $I_{ev}/(I_{pr}+I_{ev})$ as a function of the propagation distance z; (b) $(I_{ev})_L/(I_{ev})_T$ as a function of the waist size w in the interval $[0.01\lambda,\lambda]$.

spatial variations of evanescent wave in x and y components. Furthermore, the coherent superposition of the evanescent wave in x and y components gives rise to the increase of I_{ev}, as recognized from Eqs. (4) and (5).

The longitudinal component cannot be neglected in the near field for a highly nonparaxial case. Since the evanescent wave component dominates the near field, we thus discuss the contributions of the longitudinal and transverse components in the evanescent wave part with the highly nonparaxial case ($w = 0.1\lambda$). Their relative contributions can be compared by the ratio of $(I_{ev})_L/(I_{ev})_T$. $(I_{ev})_T$ and $(I_{ev})_L$ are the transverse and longitudinal plane-integrated intensities of the evanescent wave, respectively, which are expressed as

$$(I_{ev})_T = 2\pi \int_1^\infty |T|^2 |P|^2 \frac{3\rho^3 - 2\rho}{2\rho^2 - 1} d\rho, \tag{11}$$

$$(I_{ev})_L = 2\pi \int_1^\infty |T|^2 |P|^2 \frac{\rho^5}{2\rho^4 - 3\rho^2 + 1} d\rho. \tag{12}$$

As described in the above equations, the transverse and longitudinal contributions are described by the plane-wave spectrum. According to the Parseval theorem, the values $(I_{ev})_T$ and $(I_{ev})_L$ keep invariant when propagating in free space. By obtaining the $(I_{ev})_L/(I_{ev})_T$ ratio of the initial plane, it is therefore sufficient to compare the relative contributions of the longitudinal and transverse components. The ratio $(I_{ev})_L/(I_{ev})_T$ versus the waist size w is shown in Fig. 4(b). The ratio $(I_{ev})_L/(I_{ev})_T$ is enhanced with the increase of w and then is saturated at a certain value w as shown in Fig. 4(b). Furthermore, the value w for the saturation shifts to a higher value and the ratio $(I_{ev})_L/(I_{ev})_T$ decreases when the topological charge number of polarization m increases as shown in Fig. 4(b).

In order to further explore the properties of the spin-orbital AM conversion, an understanding of the vectorial structure in the near field is important to gain insight into the properties of the evanescent and propagating waves. The comparison between the longitudinal and transverse components of the propagating and evanescent waves, as well as the transverse energy flux of the propagating and evanescent waves in the near field is analyzed, as shown in Fig. 5. For the longitudinal components, it is found that the reshaped intensity distributions of the evanescent wave are the same as that of the propagating wave component. In addition, the spatial size of the evanescent wave is smaller than that of the propagating wave. It is interesting to note that the longitudinal components of the reshaped intensity distribution are different than that of their corresponding transverse components. The reshaping of the intensity distribution of the longitudinal components of the evanescent wave is attributed to the SOP distribution in the field cross section. The evanescent waves dominate the field in near field and sensitively depend on the distribution of SOP in the field cross section as shown in Fig. 5. The transverse energy flux induced by the longitudinal component of both evanescent and propagating waves leads to the appearance of the orbital angular momentum.

IV. CONCLUSION

The spin-to-orbital angular momentum conversion in the longitudinal components of a vector optical field with hybrid SOP in the near field is studied in detail. The underlying physics are explored by examining the longitudinal component with the 3D vectorial structure of a high nonparaxial beam. The spatial shapes of the intensity distribution of the longitudinal components are different than that of the transverse components, and they depend sensitively on the number of polarization topological charges and the SOP distribution. The distribution of SOP in the field cross section reshapes the intensity and the phase distributions of the longitudinal component. The ability to manipulate the intensity and the phase distributions of the longitudinal component by controlling the SOP distributions leads to the more flexible control of the spin-to-orbital angular momentum conversion scenarios of a highly nonparaxial beam with hybrid SOP in the near field. The spin-orbital AM conversion in the near field of a highly nonparaxial vector beam discussed in the present work is different from the usual method of spin-orbital AM conversion by using a q-plate convertor [15]. Practically, to obtain a highly nonparaxial vector beam with hybrid SOP is the key to realize the spin-orbit AM conversion as described in this present approach. However, it is difficult to obtain such a highly nonparaxial vector optical field in subwavelength scale. One possible approach is to generate the highly nonparaxial vector optical field in nanoscale by designing a

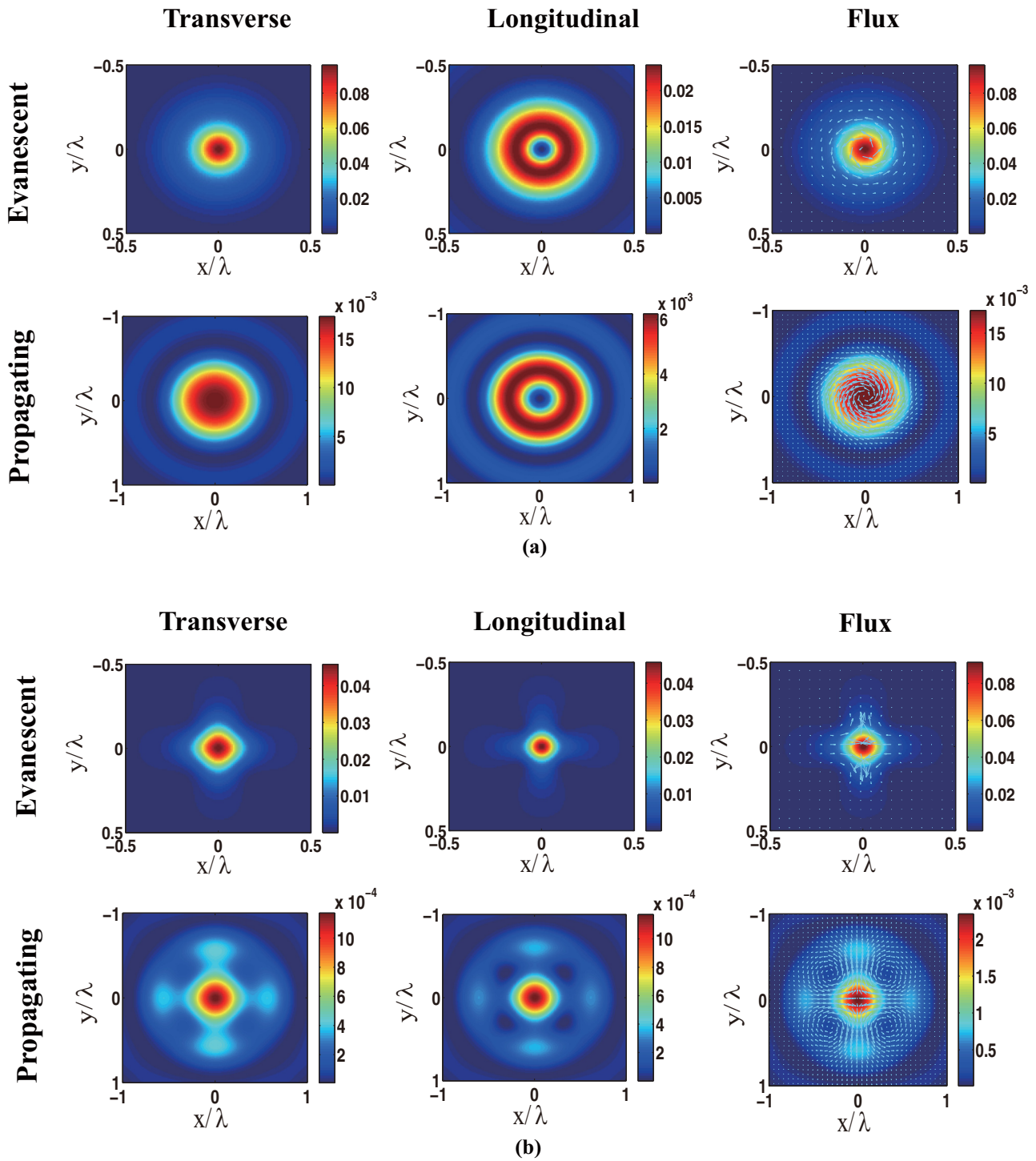

FIG. 5. Transverse component, longitudinal component, and transverse energy flux density distributions of the evanescent wave and propagating wave for an optical field with (a) circular polarization and (b) $m = 1$, $\theta_0 = 0$, and $\Delta\theta = \pi/2$ for the hybrid SOP. The waist size $w = 0.1\lambda$ and propagation distance $z = 0.1\lambda$. Here the coordinate unit is wavelength λ. The intensity distributions have been normalized to the initial peak intensity.

microstructure metasurface [45]. Another feasible approach is to generate the highly nonparaxial vector field in electromagnetic wave regime [30,31]. Once the highly nonparaxial beam with hybrid SOP is generated, the spin-orbital AM conversion can occur in the longitudinal component in the near field.

ACKNOWLEDGMENTS

This work is supported by the Zhejiang Provincial Natural Science Foundation under Grant No. LZ17A040001, the National Natural Science Foundation of China (Grant No. 11574271), and the Science Research Foundation of Zhejiang Sci-Tech University (ZSTU) under Grant No. 14062078-Y.

[1] L. Allen, M. W. Beijersbergen, R. J. C. Spreeuw, and J. P. Woerdman, Phys. Rev. A **45**, 8185 (1992).
[2] A. T. O'Neil, I. MacVicar, L. Allen, and M. J. Padgett, Phys. Rev. Lett. **88**, 053601 (2002).
[3] G. C. G. Berkhout, M. P. J. Lavery, J. Courtial, M. W. Beijersbergen, and M. J. Padgett, Phys. Rev. Lett. **105**, 153601 (2010).
[4] K. Dholakia and T. Čižmár, Nat. Photon. **5**, 335 (2011).
[5] M. Padgett and R. Bowman, Nat. Photon. **5**, 343 (2011).
[6] L. Paterson *et al.*, Science **292**, 912 (2001).
[7] K. Y. Bliokh, M. A. Alonso, E. A. Ostrovskaya, and A. Aiello, Phys. Rev. A **82**, 063825 (2010).
[8] F. Töppel *et al.*, New J. Phys. **16**, 073019 (2014).
[9] A. Aiello *et al.*, New J. Phys. **17**, 043024 (2015).
[10] X. F. Qian and J. H. Eberly, Opt. Lett. **36**, 4110 (2011).
[11] J. Petersen, J. Volz, and A. Rauschenbeutel, Science **346**, 67 (2014).
[12] D. O'Connor *et al.*, Nat. Commun. **5**, 5327 (2014).
[13] M. Righini, G. Volpe, C. Girard, D. Petrov, and R. Quidant, Phys. Rev. Lett. **100**, 186804 (2008).
[14] M. Li *et al.*, Nat. Nanotechnol. **5**, 570 (2010).
[15] L. Marrucci, C. Manzo, and D. Paparo, Phys. Rev. Lett. **96**, 163905 (2006).
[16] M. Sukharev and T. Seideman, Nano Lett. **6**, 715 (2006).
[17] C. E. R. Souza and A. Z. Khoury, Opt. Express **18**, 9207 (2010).
[18] W. T. Buono *et al.*, New J. Phys. **16**, 093041 (2014).
[19] Y. Zhao, J. S. Edgar, G. D. M. Jeffries, D. McGloin, and D. T. Chiu, Phys. Rev. Lett. **99**, 073901 (2007).
[20] F. D. Fornel, *Evanescent Waves: From Newtonian Optics to Atomic Optics* (Springer, Berlin, 2001).
[21] G. P. Agrawal and M. Lax, Phys. Rev. A **27**, 1693 (1983).
[22] N. I. Petrov, J. Opt. Soc. Am. A **20**, 2385 (2003).
[23] H. Chen *et al.*, Opt. Lett. **36**, 3179 (2011).
[24] R. P. Chen *et al.*, Sci. Rep. **5**, 10628 (2015).
[25] X. L. Wang *et al.*, Opt. Express **18**, 10786 (2010).
[26] R. P. Chen *et al.*, Laser Photon. Rev. **11**, 1700165 (2017).
[27] R. P. Chen *et al.*, Opt. Express **24**, 28143 (2016).
[28] R. P. Chen and C. Q. Dai, Nonlin. Dyn. **88**, 2807 (2017).
[29] C. Rizza, A. Ciattoni, and E. Palange, Opt. Express **18**, 7617 (2010).
[30] R. Merlin, Science **317**, 927 (2007).
[31] A. Grbic, L. Jiang, and R. Merlin, Science **320**, 511 (2008).
[32] R. P. Chen and G. Li, Opt. Express **21**, 22246 (2013).
[33] R. P. Chen *et al.*, Chin. Phys. B **26**, 104202 (2017).
[34] G. C. Sherman, J. J. Stamnes, and E. Lalor, J. Math. Phys. **17**, 760 (1976).
[35] M. V. Berry, Proc. SPIE **3487**, 6 (1998).
[36] R. Martínez-Herrero and P. M. Mejías, Opt. Express **18**, 7965 (2010).
[37] C. G. Darwin, Proc. R. Soc. A **136**, 36 (1932).
[38] X.-L. Wang, J. Chen, Y. Li, J. Ding, C.-S. Guo, and H.-T. Wang, Phys. Rev. Lett. **105**, 253602 (2010).
[39] K. Y. Bliokh and F. Nori, Phys. Rep. **592**, 1 (2015).
[40] I. Bialynicki-Birula and Z. Bialynicka-Birula, J. Opt. **13**, 064014 (2011).
[41] I. Bialynicki-Birula, New J. Phys. **16**, 113056 (2014).
[42] L. E. Helseth, Phys. Rev. A **78**, 013819 (2008).
[43] R. Martínez-Herrero *et al.*, Appl. Phys. B **106**, 151 (2012).
[44] R. Martínez-Herrero, P. M. Mejías, and A. Carnicer, Opt. Express **16**, 2845 (2008).
[45] G. Rui and Q. Zhan, Nanophotonics **4**, 2 (2015).